iScience

CellPress

Article

Covalent Selenium Embedded in Hierarchical Carbon Nanofibers for Ultra-High Areal Capacity Li-Se Batteries

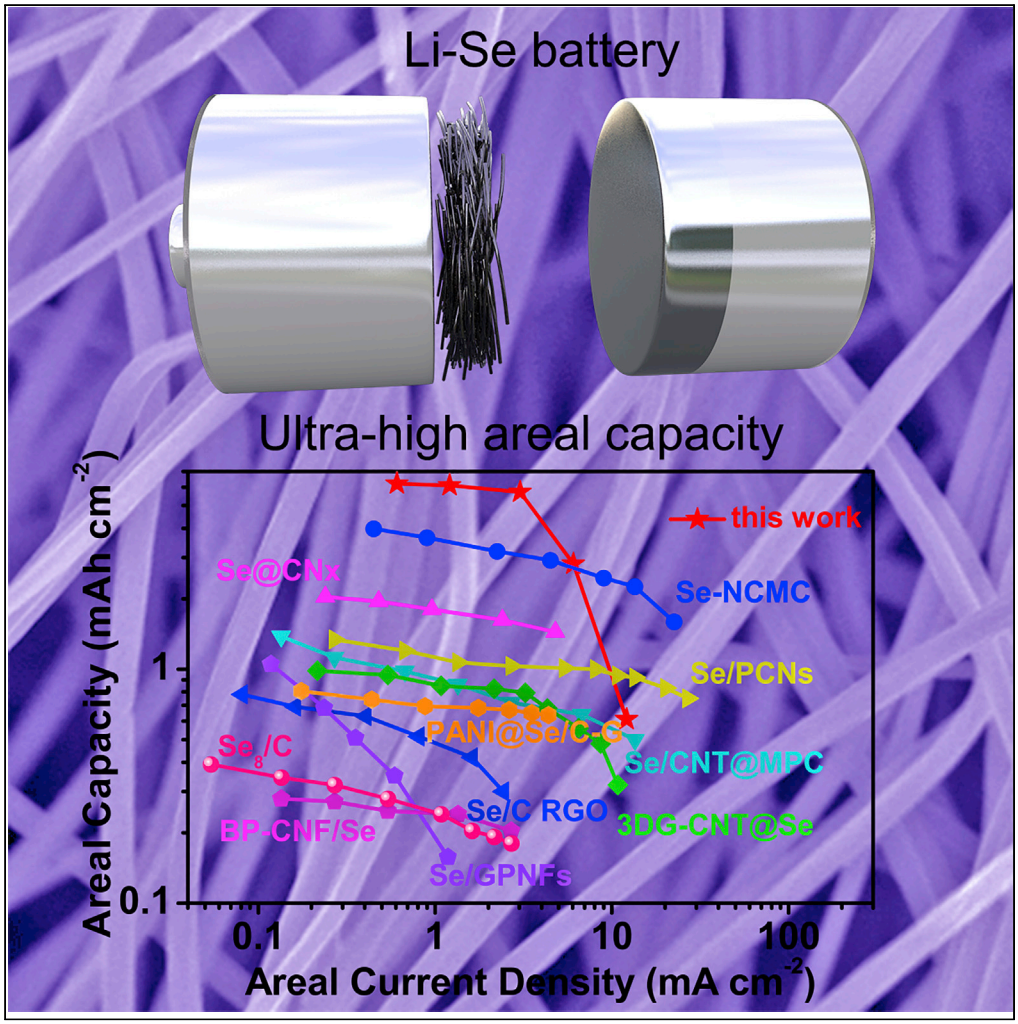

Jian Zhou, Maoxin Chen, Tao Wang, ..., Junfei Liang, Jian Zhu, Xiangfeng Duan

jzhu@hnu.edu.cn

HIGHLIGHTS

The CSe@HNCNFs were used as flexible and free-standing cathode for Li-Se battery

The CSe@HNCNFs effectively retard polyselenides diffusion during cycling

The CSe@HNCNFs delivered high areal capacity of 7.30 mAh cm^{-2}

The CSe@HNCNFs displayed excellent cyclic stability and rate performance

Zhou et al., iScience *23*, 100919
March 27, 2020
https://doi.org/10.1016/j.isci.2020.100919

iScience

CellPress

Article

Covalent Selenium Embedded in Hierarchical Carbon Nanofibers for Ultra-High Areal Capacity Li-Se Batteries

Jian Zhou,[1] Maoxin Chen,[1] Tao Wang,[1] Shengyang Li,[1] Qiusheng Zhang,[1] Meng Zhang,[1] Hanjiao Xu,[1] Jialing Liu,[1] Junfei Liang,[2,3] Jian Zhu,[1,4,*] and Xiangfeng Duan[2]

SUMMARY

Lithium selenium (Li-Se) batteries have attracted increasing interest for its high theoretical volumetric capacities up to 3,253 Ah L^{-1}. However, current studies are largely limited to electrodes with rather low mass loading and low areal capacity, resulting in low volumetric performance. Herein, we report a design of covalent selenium embedded in hierarchical nitrogen-doped carbon nanofibers (CSe@HNCNFs) for ultra-high areal capacity Li-Se batteries. The CSe@HNCNFs provide excellent ion and electron transport performance, whereas effectively retard polyselenides diffusion during cycling. We show that the Li-Se battery with mass loading of 1.87 mg cm^{-2} displays a specific capacity of 762 mAh g^{-1} after 2,500 cycles, with almost no capacity fading. Furthermore, by increasing the mass loading to 37.31 mg cm^{-2}, ultra-high areal capacities of 7.30 mAh cm^{-2} is achieved, which greatly exceeds those reported previously for Li-Se batteries.

INTRODUCTION

Lithium ion batteries (LIBs) represent the primary energy storage technology that is critical for mobile electronics and electric vehicles (Sun et al., 2017, 2019; Liang et al., 2019). There is considerable interest in developing newer generation of energy storage devices that may deliver higher energy density, higher power density, and longer cycle life than the current state-of-the-art LIBs. Lithium-sulfur (Li-S) batteries have received significant recent attention for their high theoretical energy density, high earth abundance, low cost, and eco-friendliness (Cheng et al., 2018). Unfortunately, there are several inherent obstacles toward the practical application of Li-S batteries including low utilization ratio of sulfur, serious polysulfide shuttling effect, and rapid capacity decay (Zhang et al., 2010; Tao et al., 2016; Park et al., 2015).

Li-Se batteries are considered as an interesting alternative to Li-S batteries because of similar chemical properties and theoretical volumetric capacity (Li_2Se, 3,253 Ah L^{-1}), higher electronic conductivity (10^{-3} S m^{-1}), higher active material utilization, and better rate capability (Luo et al., 2013). However, Li-Se batteries also undergo serious polyselenides (PSes, Li_2Se_x, $4 \leq x \leq 8$) ''shuttle effect,'' thus leading to irreversible capacity loss (Abouimrane et al., 2012; Yang et al., 2013; Han et al., 2014; Luo et al., 2014). To overcome this challenge, a variety of carbon materials with loading active selenium have been reported, including porous carbon spheres (Luo et al., 2013; Li et al., 2014), carbon nanotubes (Han et al., 2014; He et al., 2016), and so on, to trap PSes in pores and improve the electrochemical properties of Li-Se batteries (Ding et al., 2018). However, the current studies that are largely limited to electrodes with rather low mass loading and low areal capacity cannot satisfy the practical application.

To simultaneously achieve high power density and high energy density requires ideal electrode structures that can rapidly release enough charges (electrons and ions) within a given charge-discharge period, as well as store abundant charges (such as lithium ions). This situation can be easily achieved under relatively thin films and nano-scale material electrodes with low mass loading (<1 mg cm^{-2}) (Li et al., 2014, 2015). Nevertheless, as thickness of the electrode increases, the limitation of ion diffusion becomes more serious, so it is difficult to reach the mass loading of industrial application (~10 mg cm^{-2}) (Singh et al., 2015). Enhancing areal capacity by increasing areal mass loading may seem straightforward. There also has been limited success so far due to some key challenges related to the intrinsic nature of Se/C composites (Abouimrane et al., 2012; Yang et al., 2013; Han et al., 2014; Luo et al., 2014). Up to now, the reported highest areal mass loading and areal capacity of Li-Se batteries are 6.64 mg cm^{-2} and 4.12 mAh cm^{-2},

[1]State Key Laboratory for Chemo/Biosensing and Chemometrics, College of Chemistry and Chemical Engineering, and Hunan Key Laboratory of Two-Dimensional Materials, Hunan University, Changsha 410082, P. R. China

[2]Department of Chemistry and Biochemistry, University of California, Los Angeles, CA 90095, USA

[3]School of Energy and Power Engineering, North University of China, Taiyuan, Shanxi 030051, P. R. China

[4]Lead Contact

*Correspondence: jzhu@hnu.edu.cn

https://doi.org/10.1016/j.isci.2020.100919

respectively (Ding et al., 2018). In addition, due to the presence of other passive components such as current collectors, binders, and conductive additives in the practical device, the excellent electrochemical performance of the Li-Se batteries may be reduced rapidly (Gogotsi and Simon, 2011). Therefore, it has been rarely reported that mass loading or areal capacities of energy storage devices is higher than that of currently available LIBs (Kalimuthu and Nallathamby, 2018; Yang et al., 2013; Zhang et al., 2017;Zeng et al., 2015; Hong et al., 2018).

Here, we reported an architecture of covalent selenium embedded in hierarchical N-doped carbon nanofibers (CSe@HNCNFs) as flexible, free-standing, and binder-free cathode for Li-Se batteries. The CSe@HNCNFs with hierarchically porous structure (micro/meso/macro-pores and nano-channels), high-content nitrogen doping, and robust covalent bonds (Se-O and Se-C) can not only facilitate the rapid transport of ions and electrons throughout the entire electrode architecture but also effectively anchor PSes diffusion and afford built-in void space to tolerate the volume change during cycling. Thus, excellent electrochemical performance was achieved under different mass loading (from 1.52 to 37.31 mg cm^{-2}). When mass loading was 1.52 mg cm^{-2}, a high specific capacity of 412 mAh g^{-1} (normalized by the mass of Se) could be maintained under current density of 40.61 mA cm^{-2}. Moreover, the composite cathode with high mass loading up to 37.31 mg cm^{-2} delivered a high areal capacity of 7.30 mAh cm^{-2} (the highest areal capacity among all the Li-Se batteries) at a current density of 0.83 mA cm^{-2}. This work represents a critical step toward capturing high-areal-capacity Li-Se batteries to meet practical devices.

RESULTS

Preparation and Structure of CSe@HNCNFs Composite

In the specific synthesis process, polyacrylonitrile (PAN) and polymethylmethacrylate (PMMA) were used as carbon source and pore-forming agent, respectively. PAN/PMMA nanofiber film was obtained by electrospinning and then pre-oxidized at 280°C. During the pre-oxidized process, the PMMA was decomposed, leading to formation of nano-channel and porous structure within the nanofiber film. After that, selenium powder sprinkled on pre-oxidized PAN fabric was encapsulated in a vacuum quartz bottle and then annealed in a tubular furnace (Figure S1). It is worth noting that it is much easier to form covalent bonds with selenium vapor during annealing process due to a large number of unsaturated bonds of the pre-oxidized PAN and high reactivity of selenium at high temperature (Liu et al., 2017; Yang et al., 2018). Thus, the CSe@HNCNFs with hierarchically porous structure (micro/meso/macro-pores and nano-channels) and robust covalent bonds were obtained through the unique synthetic strategy.

The CSe@HNCNFs film with strong mechanical robustness and flexibility was cut into a 12 mm disc and directly used as cathode for Li-Se batteries (Figure 1A). Scanning electron microscopy (SEM) images in Figures 1B and 1C show that uniform fibers in CSe@HNCNFs composite with diameter around 300 nm and smooth surface interwove to form a good conductive network, therefore guaranteeing fast electron conduction. As displayed in Figure S2, the CSe@HNCNFs show similar morphology with pure HNCNFs. As seen from side-view SEM image of a single fiber in Figure 1C a hierarchically porous structure can be clearly observed, corresponding to transmission electron microscopy (TEM) images of CSe@HNCNFs (Figures 1D and 1E). The CSe@HNCNFs with hierarchically porous structure can not only accelerate penetration of electrolyte but also buffer volume expansion during charge-discharge process. Besides, high-resolution transmission electron microscopy (HRTEM) image and corresponding selected area electron diffraction (SAED) pattern in Figure 1F indicate that the selenium in the CSe@HNCNFs is in amorphous state. As presented in Figures 1G–1D, elemental mappings of CSe@HNCNFs suggest that the C, O, N, and Se are homogeneously distributed in CSe@HNCNFs.

The microstructure of the as-prepared materials was further analyzed by X-ray diffraction (XRD). Figure 2A displays that diffraction pattern of pure selenium exhibits an equilibrium trigonal crystal system $P3_121$. The typical peaks of Se are obviously absent in CSe@HNCNFs and HNCNFs patterns, also suggesting a highly scattered amorphous state of selenium, leading to high utilization rate during the process of electrochemical (Li et al., 2015). The peaks of carbon at about 24° and 43° in XRD patterns of the CSe@HNCNFs shift to the left compared with that of HNCNFs due to increased lattice constant caused by selenium doping in CSe@HNCNFs. As shown in Figure 2B, two characteristic peaks located at 1,340 and 1,580 cm^{-1} in CSe@HNCNFs and HNCNFs patterns correspond to the disordered carbon (I_D) and the ordered graphite lattice (I_G), respectively. The I_D/I_G of CSe@HNCNFs and HNCNFs showed almost the same ratio, indicating that the addition of selenium can hardly affect defect or disorder degree of HNCNFs. Because the Raman

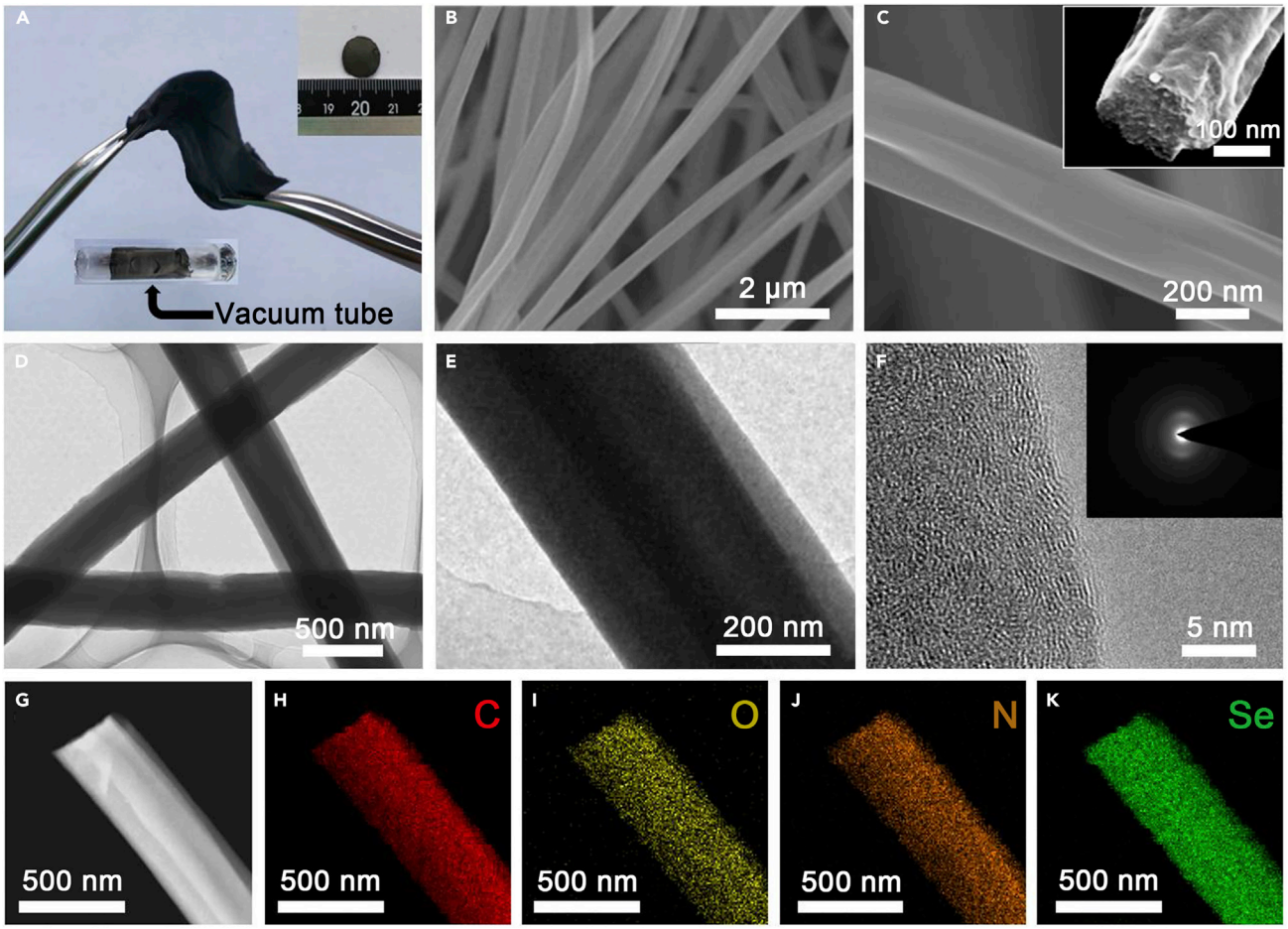

Figure 1. Morphological Characterizations of the HNCNFs and CSe@HNCNFs Composites

(A) Digital photograph of flexible and free-standing CSe@HNCNFs electrode.

(B and C) (B) Low-magnification and (C) high-magnification SEM images of CSe@HNCNFs composite (microstructure of the cross section displayed in the insert).

(D and E) (D) Low-magnification and (E) high-magnification TEM images of CSe@HNCNFs composite.

(F) HRTEM images of CSe@HNCNFs composite and corresponding SAED pattern.

(G–K) (G) TEM image and elemental mappings (carbon (H), oxygen (I), nitrogen (J), selenium (K)) of CSe@HNCNFs composite.

spectrum collects signals from the material surface, no obvious Raman peak of the pure selenium was found in the CSe@HNCNFs composite, which further proves the perfect expansion of selenium into HNCNFs (Li et al., 2015). X-ray photoelectron spectroscopy (XPS) was used to study the chemical composition of CSe@HNCNFs. Figure 2C shows pronounced O 1s, N 1s, C 1s, Se 3s, Se 3p, and Se 3d peaks at about 533.4, 400.7, 284.8, 229.6, 161.6, and 55.6 eV, respectively. A main peak of 284.8 eV in the high-resolution C 1s spectrum in Figure 2D can be divided into four kinds of peaks at 284.8, 286.7, 288.5, and 291.6 eV, corresponding to the C=C/C-C, C-N/C-O, C=O, and C=O, respectively (Wang et al., 2019; Li et al., 2016). Figure 2E presents Se 3d spectra of pristine Se and CSe@HNCNFs with the $3d_{5/2}$ and $3d_{3/2}$ peaks located at 56.06 and 55.20 eV, respectively. The spin orbitals are divided at 0.86 eV, whereas the $3d_{5/2}$ and $3d_{3/2}$ peaks of Se transfer to higher binding energies in CSe@HNCNFs compared with the $3d_{5/2}$ and $3d_{3/2}$ peaks of pure Se at 56.06 and 55.20 eV, respectively (Luo et al., 2013; Zhang et al., 2014). This shift is due to change in the density of selenium's electron cloud, indicating selenium formed bonds with other atoms (C and O) in the composite (Hong et al., 2018; Xin et al., 2016; Babu et al., 2007; Luo et al., 2015). Similarly, a wide peak of Se 3d with low strength at about 58.50 eV is due to the forming of Se-O or Se-C (Li et al., 2015). In addition, the N 1s spectra (Figure 2F) of CSe@HNCNFs shows the presence of graphite N (400.1 eV), pyrrolic N (399.2 eV), and pyridine N (398.2 eV) (Zhang et al., 2019; Delamar et al., 1992). The elemental content of N in CSe@HNCNFs is as high as 12.66%. The N-doping can greatly improve

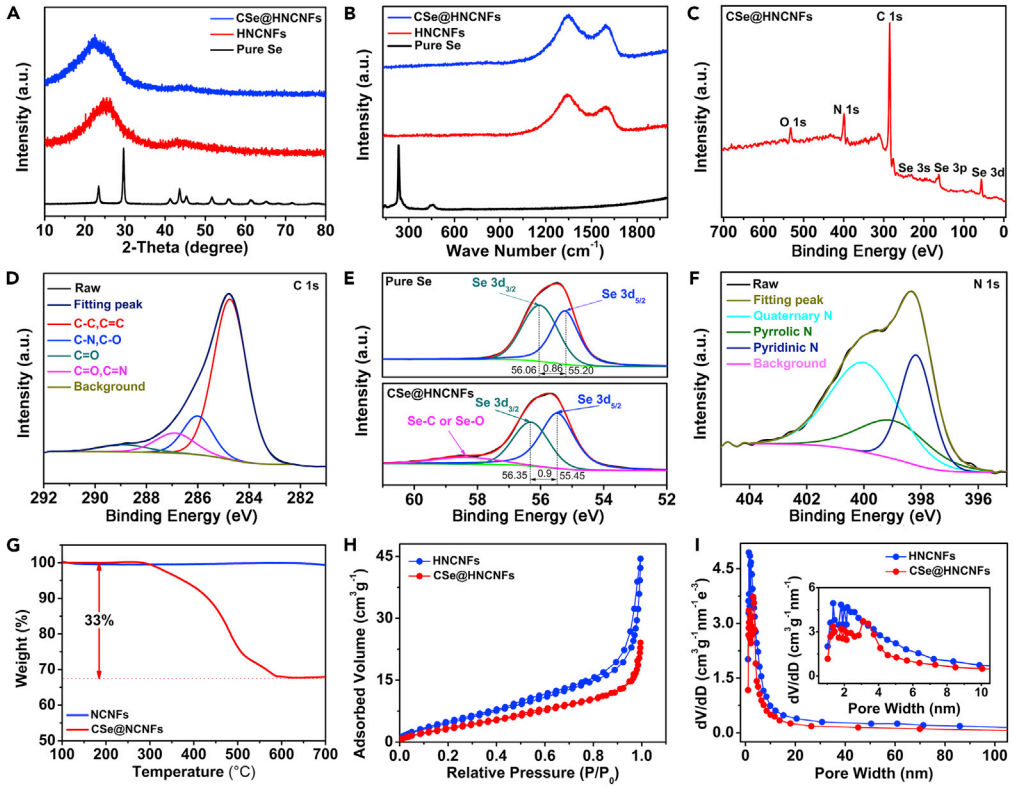

Figure 2. Composed Characterization of HNCNFs and CSe@HNCNFs Composites

(A and B) (A) XRD patterns and (B) Raman spectra of the pristine Se powder, HNCNFs, and CSe@HNCNFs.

(C) XPS survey spectra of CSe@HNCNFs.

(D) High-resolution XPS spectra of C 1s for CSe@HNCNFs.

(E) High-resolution XPS spectra of Se 3d for pure Se and CSe@HNCNFs.

(F) High-resolution XPS spectra of N 1s for CSe@HNCNFs.

(G) TG profiles of the obtained composite of CSe@HNCNFs versus HNCNFs.

(H and I) (H) N_2 adsorption-desorption isothermal curves and (I) corresponding pore-size distribution curves of HNCNFs and CSe@HNCNFs.

the conductivity of this composite and thus improve the rate performance of the electrode (Ania et al., 2007; Biniak et al., 1997; Jiang et al., 2015). Thermogravimetric (TG) profiles were used to study weight ratio of selenium in the composite. As shown in Figure 2G, The weight loss of CSe@HNCNFs can be divided into two scopes, including a rapid weight loss scope between 280 and 520°C and a slow weight loss scope over 520°C. The rapid and slow weight loss scopes are attributed to the different breakdown temperature of the Se-Se and the Se-C (Se-O) bonds, respectively (Zhang, 2014). Thus, the content of selenium in the carbon matrix is determined to be about 33%, and the maximum selenium loading corresponding to the area of the independent electrode is determined to be 12.31 mg cm^{-2}. After Se loading in HNCNFs, specific surface area of HNCNFs decreases from 19.4 to 13.7 $m^2 g^{-1}$ (Figure 2H), and pore-size distribution of micro-porous region (<2 nm) and mesoporous region (2–50 nm) decreases significantly (Figure 2I) due to the permeation of Se in the hierarchical structure of HNCNFs matrix.

Electrochemical Evaluation of the CSe@HNCNFs Electrodes

To explore electrochemical performance of CSe@HNCNFs cathode, 2032-type coin cell was assembled with lithium metal as anode and CSe@HNCNFs film as cathode. Figures 3A and 3B show cyclic voltammograms (CV) and charge-discharge curves, respectively. During the first discharge cycle, two obvious cathode peaks at 1.52 and 1.27 V indicate that the conversion from Se to Li_2Se experienced two-step reactions (Se → Li_2Se_x → Li_2Se, $x \geq 4$) (Luo et al., 2013; Yang et al., 2013; Xin et al., 2012). However, only one peak appears in the cathode segment in the following cycles, which can be ascribed to the conversion of Se to Li_2Se. This is very owing to the irreversible reduction peak (1.52 V), which only appears in the first cycle and disappears in the follow cycles. The

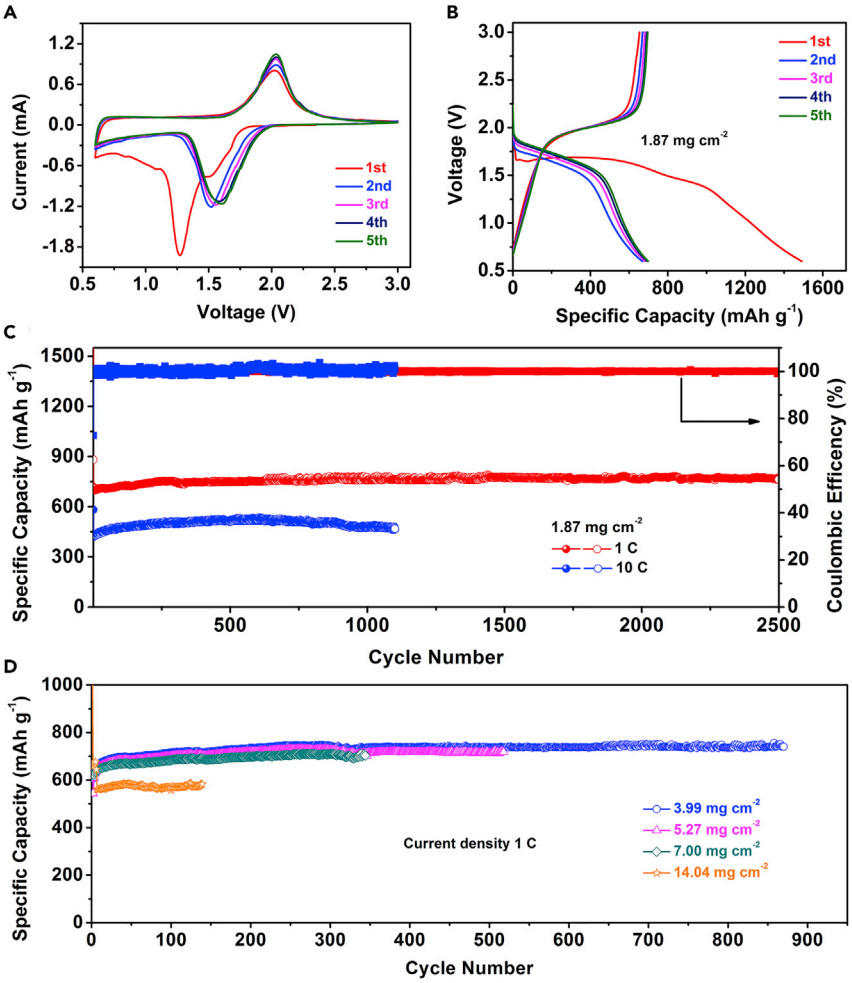

Figure 3. Electrochemical Properties of Li-Se Cells with a CSe@HNCNFs Electrode

(A) Cyclic voltammograms for the first five cycles obtained at 0.1 mV s^{-1}.

(B) Galvanostatic charge-discharge curves of the CSe@HNCNFs electrode at the rate of 1 C with the mass loading of 1.87 mg cm^{-2}.

(C) Cycling performances and Coulombic efficiencies of the CSe@HNCNFs electrode at rates of 1 and 10 (C).

(D) Cycling performances of CSe@HNCNFs electrode at the rate of 1 C under different mass loadings of 1.87, 3.99, 5.27, 7.00, and 14.04 mg cm^{-2}.

irreversible reduction peak (1.52 V) corresponds to the process of trace amount of cyclic Se_8 in nano-channels or on the surface of hierarchically porous nanofibers forming soluble polyselenides, Li_2Se_x ($x \geq 4$), and shuttling into the electrolyte (Yang et al., 2013). It is worth noting that the remaining Se exists as an amorphous state with only conversion reaction of Se to Li_2Se during the discharge process, indicating only one peak appears in the cathode segment in the following cycles (Yang et al., 2013; Li et al., 2014). As the cycle continues, the peak moves to high voltage and overlaps from the fourth cycle. In the charge cycle, only one anode peak at around 2.0 V indicates one-step reversible transformation from Li_2Se to Se. Consistent with CV results, there is only one platform from the second charge-discharge curve. After the first three cycles, the charge-discharge curves almost overlap, implying a highly reversible electrochemical reaction and an excellent cycling stability. In Figure 3B, the cell exhibits a low initial Coulomb efficiency (ICE), which is attributed to the following two reasons. First, the pure HNCNFs electrodes displaying low Coulombic efficiency at same current density, similar to previous report, is one of the reasons for the extremely low ICE (Yang et al., 2013). Second, the formation of an irreversible solid electrolyte interface (SEI) on the surface of anode would also cause low initial Coulombic efficiency (Luo et al., 2013). Figure 3C is the cycling performance of CSe@HNCNFs electrode under current rate (C-rate) of 1 and 10 C (1 C = 675 mA g^{-1}). It should be noted that the N-doped carbon host provides negligible specific capacities of 49.5 and 21.1 mAh g^{-1} at 0.1 and 1 A g^{-1}, respectively (Figure S3). When the circulating current rates are 1 and 10 C, specific capacities of

762 and 465 mAh g^{-1} are obtained after 2,500 and 1,100 cycles, respectively, with almost no attenuation in capacity. Coulombic efficiency reaches more than 99.5% since the fifth cycle, indicating an outstanding electrochemical reversibility of the CSe@HNCNFs electrode. Moreover, the morphology, composition, and chemical state of CSe@HNCNFs composite are shown as Figure S4 after cycling. The morphology and composition display almost no change compared with that before cycling (Figures S4A–S4C). The XPS investigations in Figures S4D–S4F show that high-resolution C 1s, Se 3d spectra, and N 1s spectra suggest almost same chemical state of CSe@HNCNFs electrode before and after cycling (Figures 2D–2F). In addition, the proportion of C=O, Se-C, and Se-O bonds increased after cycling, which was attributed to electrolyte decomposition and dissolution of polyselenium compounds. Figure 3C exhibits a continuous rise of the reversible capacity during the first 300 cycles, which may be ascribed to the hysteresis of electrolyte infiltrating in the hierarchically porous matrix and the reduced internal impedance (Figure S5). Meanwhile, we also conducted a series of long cycling test of CSe@HNCNFs electrodes with different mass loading at the C-rate of 1 C (Figure 3D). When the mass loads are 3.99, 5.27, and 7.00 mg cm^{-2}, high specific capacities of 740.5, 717.8, and 702.8 mAh g^{-1} can be obtained even after 870, 520, and 350 cycles, respectively. Moreover, the CSe@HNCNFs electrode with a high mass loading of 14.04 mg cm^{-2} shows a high specific capacity of 582 mAh g^{-1}. In addition, a series of long cycling test of CSe@HNCNFs electrodes are conducted at different C-rates with mass loading of 1.79 mg cm^{-2} (Figure S6). Apparently, the CSe@HNCNFs electrode demonstrates superior cyclic stability at different mass loading. On one hand, the CSe@HNCNFs electrode with hierarchically porous structure can effectively buffer volume change of Se and offer outstanding ion and electron transport performance. On the other hand, the CSe@HNCNFs with the amorphous selenium bonding tightly with the HNCNFs host through Se-O or Se-C, and C-O bonds can immobilize PSes and prevent the active selenium transferring from the electrode to the electrolyte, thus improving the cycle stability of Li-Se battery (Li et al., 2015). We believe the covalent bonds coupled with the hierarchically porous N-doped host can be also extended to Li-S batteries (Zhang, 2014; Talapaneni et al., 2016).

Charge and discharge curves of CSe@HNCNFs electrode in Figure 4A exhibits no significant voltage drop and capacity loss with the increase of mass loading. This may be attributed to the low internal resistance and outstanding structural stability of CSe@HNCNFs electrode. Figure 4B displays charge-discharge profiles of CSe@HNCNFs electrode with a mass loading of 1.52 mg cm^{-2} at different current rates. When the rates are 0.2, 0.5, 1, 2, 5, 10, 20, and 50 C, the corresponding specific capacities are 773.4, 726.2, 699.4, 658.7, 601.6, 547.6, 489.4, and 414 mAh g^{-1}, respectively. Even if the current density increases 250 times, the specific capacity maintenance rate is still as high as 54% compared with that at the current density of 0.2 C. Figure 4C shows charge-discharge curves of CSe@HNCNFs electrode with ultra-high mass loading level of about 27.12 mg cm^{-2} at different C-rates. The reversible capacity of the CSe@HNCNFs electrode is 699 mAh g^{-1} at current rate of 0.1 C. When the rate increases to 0.2, 0.5, and 1 C, the corresponding specific capacities are as high as 680.4, 636.8, and 334.8 mAh g^{-1}, respectively. Figure 4D shows rate performance under different mass loadings. The CSe@HNCNFs electrode with various mass loadings displays unconspicuous capacity fading at C-rates of 0.2, 0.5, 1, 2, and 5 C, displaying an excellent electrochemical reversibility. Particularly noteworthy is that the CSe@HNCNFs with a mass loading of 1.52 and 3.63 mg cm^{-2} deliver high specific capacity of 414.0 and 150.7 mAh g^{-1} at ultrahigh current rate of 50 C. The CSe@HNCNFs electrode with various mass loadings can also deliver high specific reversible capacity after the C-rate returns to 1, 0.5, and 0.2 C. Moreover, Figure 4E shows capacities versus cycle number of CSe@HNCNFs electrode with ultrahigh mass loading of 27.12 mg cm^{-2} at various charge-discharge C-rates ranging from 0.1 to 2 C. The retention rate of specific capacity can still reach 42% at high current density of 6.07 mA cm^{-2} (1 C). When the current density is back to 1.21 mA cm^{-2} (0.2 C), the reversible capacity can be maintained at 6.26 mAh cm^{-2} ($\approx$700 mAh g^{-1}), indicating an outstanding tolerance of CSe@HNCNFs electrode with ultra-high mass loading to the rapid dynamics of Li-Se battery. In order to increase the mass loading of Se to make it competitive, we also measured the electrochemical performance of Li-Se batteries under higher mass loading (37.31 mg cm^{-2}) of the CSe@HNCNFs electrode. As shown in Figure S7, the CSe@HNCNFs electrode with an ultra-high mass loading of 37.31 mg cm^{-2} can still show good electrochemical performance under different current rates. The ultra-high mass loading of CSe@HNCNFs electrode enabled the Li-Se battery to display extremely high areal capacity (7.30 mAh cm^{-2}). Simultaneously, the trend graphs of the gravimetric energy density of the rate 0.2 C under different mass loads are obtained (Figure S8). The CSe@HNCNFs present high gravimetric energy density of 442.76, 402.58, 383.23, and 353.32 Wh kg^{-1} at mass loading of 1.52, 7.18, 14.37, and 27.12 mg cm^{-2}, respectively. Fast ion and electron due to N-doping hierarchically porous structure result in high utilization of materials and excellent rate capability of CSe@HNCNFs electrode. As a result, the electrode with various mass loadings displayed continuous higher areal capacities than that of previous Se based cathodes at

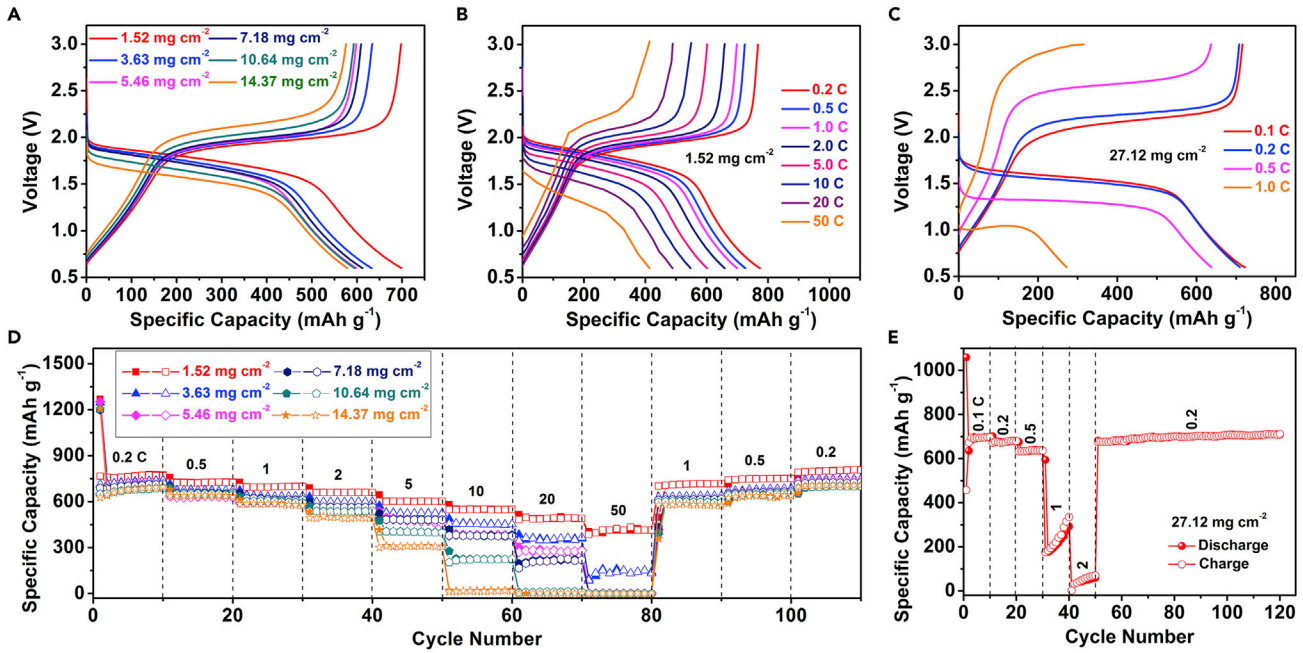

Figure 4. Rate Capability Study of CSe@HNCNFs Cathodes

(A) Galvanostatic charge-discharge curves for the CSe@HNCNFs electrode at a rate of 1 C under the mass loadings of 1.52, 3.63, 5.46, 7.18, 10.64, and 14.37 mg cm^{-2}.

(B and C) Galvanostatic charge-discharge curves for the CSe@HNCNFs electrode with mass loading of (B) 1.52 mg cm^{-2} and (C) 27.12 mg cm^{-2} the CSe@HNCNFs electrode with mass loading of mg cm^{-2} at different rates.

(D) Comparison of the rate performance of CSe@HNCNFs electrode at the current rate from 0.2 to 50 C under different mass loadings (1.52, 3.63, 5.46, 7.18, 10.64, and 14.37 mg cm^{-2}).

(E) Rate performance of CSe@HNCNFs electrode from 0.1 to 2 C when the mass loading is 27.12 mg cm^{-2}.

various current densities (Luo et al., 2013; Li et al., 2014; He et al., 2016; Ding et al., 2018; Xin et al., 2016; Cai et al., 2017; Han et al., 2015; Mukkabla et al., 2017; Wang et al., 2018; Park et al., 2018).

Increasing areal capacity is critical to achieve higher energy and power density and to reduce costs (Gallagher et al., 2016). Therefore, areal capacity is an important index to evaluate the performance of energy storage devices. The specific capacity (mAh g^{-1}) is given by the relationship between the areal capacity (mAh cm^{-2}) and the mass loading per unit area (mg cm^{-2}). As shown in Figures 4D and 4E, the C-rate and mass loading determine the specific capacity and the areal capacity. As displayed in Figure 5A, the areal capacity increases linearly until 14.37 mg cm^{-2} at C-rates of 1 and 2 C. At a higher mass loading level, deviation from linearity occurs when the areal capacity starts to reach a platform at 1 C and experiences a decrease in the areal capacity at 2 C. In the linear region, the difference of these slopes is relatively small, because the specific capacity varies very little at different mass loading levels. The platform behavior at 1 C, a sign of the penetration depth of ion current, could be explained by reaching a limit state (Gallagher et al., 2016). Figure 5B shows relationship between areal current density and areal capacity of CSe@HNCNFs electrode with different mass loading levels. An areal capacity of 6.20 mAh cm^{-2} is achieved at the high mass loading of 27.12 mg cm^{-2}. Each mass loading curve shows the shape of an arc curve: when the current density is low enough and the electrode material is easy to electrolyte infiltration, the areal capacity tends to the maximum value. When the current density increases to more than 3.10 mA cm^{-2}, the electrodes under different mass loadings show a significant decline in areal capacity. This phenomenon indicates that ion transport in electrolyte has become a limiting factor under the high current density, which leads to the decrease in areal capacity and inadequate utilization of the capacity of active electrode (Gallagher et al., 2016). In addition, Figure 5C is the comparison of areal performance metrics between CSe@HNCNFs electrode and other reported cathodes (Luo et al., 2013; Li et al., 2014; He et al., 2016; Ding et al., 2018; Xin et al., 2016; Cai et al., 2017; Han et al., 2015; Mukkabla et al., 2017; Wang et al., 2018; Park et al., 2018). It can be easy to find that when the current density is less than 6.10 mA cm^{-2}, the CSe@HNCNFs electrode delivers the highest areal capacity among all the Se-based cathodes, implying a tremendous application prospect in the field of energy-storage devices.

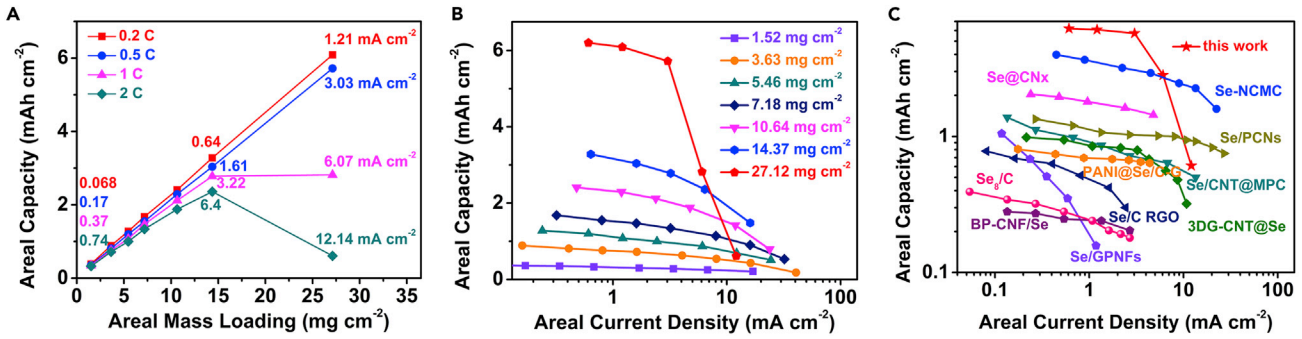

Figure 5. Performance Metrics for Electrodes with High Mass Loading

(A) The correlation of areal capacity with mass loading (1.52–27.12 mg cm^{-2}) at various C-rates for the CSe@HNCNFs electrode.

(B) The areal performance of the CSe@HNCNFs electrode under different mass loadings.

(C) The comparison of areal performance metrics between CSe@HNCNFs electrode and other Se-based reported cathodes.

DISCUSSION

In summary, we proposed a unique covalent selenium embedded in hierarchically porous N-doped carbon nanofibers for advanced Li-Se batteries. When mass loading was 1.87 mg cm^{-2}, the Li-Se batteries demonstrated a specific capacity of 762 mAh g^{-1} after 2,500 cycles at a constant current rate of 1 C, with almost no attenuation in capacity. We also studied the optimization of charge transfer and high-rate energy storage at the ultra-high mass loading level of about 37.31 mg cm^{-2} in a three-dimensional conductive bracket to obtain a particularly high areal capacity of 7.30 mAh cm^{-2} (the highest areal capacity among all the Li-Se batteries). The super-industrial mass loading and areal capacity were obtained, which can also serve as a bridge between the selenium-based cathode and Li-Se batteries for practical application.

Limitations of the Study

Although this covalently structured selenium cathode-based Li-Se batteries display long cycle, high areal capacity, and excellent rate performance, the selenium content of this selenium-based material is relatively low compared with other selenium-based materials. Therefore, future work urgently needs to find a better method that can take into account both the advantages of covalent bonds and the content of selenium.

METHODS

All methods can be found in the accompanying Transparent Methods supplemental file.

SUPPLEMENTAL INFORMATION

Supplemental Information can be found online at https://doi.org/10.1016/j.isci.2020.100919.

ACKNOWLEDGMENTS

We acknowledge the financial support from the Fundamental Research Funds for the Central Universities (No. 531118010112), the Double First-Class University Initiative of Hunan University (No.531109100004), and the Fundamental Research Funds for the Central Universities (No.531107051048). We also acknowledge the support from the Hunan Key Laboratory of Two-Dimensional Materials (No. 801200005).

AUTHOR CONTRIBUTIONS

J.Z. and X.D. designed and supervised the research; J.Z. and M.C. synthesized the material; T.W., Q.Z., and M.Z. conducted the characterization; H.X. and J.L. analyzed the data and prepared the figures. J.Z. and J.L. wrote the manuscript with input from all coauthors. All the authors participated in discussions of the research.

DECLARATION OF INTERESTS

The authors declare no competing interests.

Received: October 21, 2019
Revised: January 3, 2020
Accepted: February 11, 2020
Published: March 27, 2020

REFERENCES

Abouimrane, A., Dambournet, D., Chapman, K.W., Chupas, P.J., Weng, W., and Amine, K. (2012). A new class of lithium and sodium rechargeable batteries based on selenium and selenium-sulfur as a positive electrode. J. Am. Chem. Soc. *134*, 4505–4508.

Ania, C.O., Khomenko, V., Raymundo-Piñero, E., Parra, J.B., and Beguin, F. (2007). The large electrochemical capacitance of microporous doped carbon obtained by using a zeolite template. Adv. Funct. Mater. *17*, 1828–1836.

Babu, P.K., Lewera, A., Chung, J.H., Hunger, R., Jaegermann, W., Alonso-Vante, N., Wieckowski, A., and Oldfield, E. (2007). Selenium becomes metallic in Ru− Se fuel cell catalysts: an EC-NMR and XPS Investigation. J. Am. Chem. Soc. *129*, 15140–15141.

Biniak, S., Szymański, G., Siedlewski, J., and Świątkowski, A. (1997). The characterization of activated carbons with oxygen and nitrogen surface groups. Carbon *35*, 1799–1810.

Cai, Q., Li, Y., Li, Q., Xu, J., Gao, B., Zhang, X., Huo, K., and Chu, P.K. (2017). Freestanding hollow double-shell Se@CNxnanobelts as large-capacity and high-rate cathodes for Li-Se batteries. Nano Energy *32*, 1–9.

Cheng, Z., Xiao, Z., Pan, H., Wang, S., and Wang, R. (2018). Elastic sandwich-type rGO-VS_2/S composites with high tap density: structural and chemical cooperativity enabling lithium-sulfur batteries with high energy density. Adv. Energy Mater. *8*, 1702337.

Delamar, M., Hitmi, R., Pinson, J., and Saveant, J.M. (1992). Covalent modification of carbon surfaces by grafting of functionalized aryl radicals produced from electrochemical reduction of diazonium salts. J. Am. Chem. Soc. *114*, 5883–5884.

Ding, J., Zhou, H., Zhang, H., Tong, L., and Mitlin, D. (2018). Selenium Impregnated monolithic carbons as free-standing cathodes for high volumetric energy lithium and sodium metal batteries. Adv. Energy Mater. *8*, 1701918.

Gallagher, K.G., Trask, S.E., Bauer, C., Woehrle, T., Lux, S.F., Tschech, M., Lamp, P., Polzin, B.J., Ha, S., and Long, B. (2016). Optimizing areal capacities through understanding the limitations of lithium-ion electrodes. J. Electrochem. Soc. *163*, A138–A149.

Gogotsi, Y., and Simon, P. (2011). True performance metrics in electrochemical energy storage. Science *334*, 917–918.

Han, K., Liu, Z., Ye, H., and Dai, F. (2014). Flexible self-standing grapheme-Se@ CNT composite film as a binder-free cathode for rechargeable Li-Se batteries. J. Power Sources *263*, 85–89.

Han, K., Liu, Z., Shen, J., Lin, Y., Dai, F., and Ye, H. (2015). A free-standing and ultralong-life lithium-selenium battery cathode enabled by 3D mesoporous carbon/graphene hierarchical architecture. Adv. Funct. Mater. *25*, 455–463.

He, J., Chen, Y., Lv, W., Wen, K., Li, P., Wang, Z., Zhang, W., Qin, W., and He, W. (2016). Three-dimensional hierarchical graphene-CNT@ Se: a highly efficient freestanding cathode for Li-Se batteries. ACS Energy Lett. *1*, 16–20.

Hong, Y.J., Roh, K.C., and Kang, Y.C. (2018). Mesoporous graphitic carbon microspheres with a controlled amount of amorphous carbon as an efficient Se host material for Li-Se batteries. J. Mater. Chem. A *6*, 4152–4160.

Jiang, Y., Ma, X., Feng, J., and Xiong, S. (2015). Selenium in nitrogen-doped microporous carbon spheres for high-performance lithium-selenium batteries. J. Mater. Chem. A *3*, 4539–4546.

Kalimuthu, B., and Nallathamby, K. (2018). Optimization of structure and porosity of nitrogen containing mesoporous carbon spheres for effective selenium confinement in futuristic lithium-slelenium batteries. ACS Appl. Mater. Interfaces *6*, 7064–7077.

Li, Z., Yuan, L., Yi, Z., Liu, Y., and Huang, Y. (2014). Confined selenium within porous carbon nanospheres as cathode for advanced Li-Se batteries. Nano Energy *9*, 229–236.

Li, X., Liang, J., Hou, Z., Zhang, W., Wang, Y., Zhu, Y., and Qian, Y. (2015). A new salt-baked approach for confining selenium in metal complex-derived porous carbon with superior lithium storage properties. Adv. Funct. Mater. *25*, 5229–5238.

Li, G., Sun, J., Hou, W., Jiang, S., Huang, Y., and Geng, J. (2016). Three-dimensional porous carbon composites containing high sulfur nanoparticle content for high-performance lithium-sulfur batteries. Nat. Commun. *7*, 10601.

Liang, J., Sun, H., Zhao, Z., Wang, Y., Feng, Z., Zhu, J., Guo, L., Huang, Y., and Duan, X. (2019). Ultra-high areal capacity realized in three-dimensional holey graphene/SnO_2 composite anodes. iScience *19*, 728–736.

Liu, Y., Tai, Z., Zhang, Q., Wang, H., Pang, W.K., Liu, H.K., Konstantinov, K., and Guo, Z. (2017). A new energy storage system: rechargeable potassium-selenium battery. Nano Energy *35*, 36–43.

Luo, C., Xu, Y., Zhu, Y., Liu, Y., Zheng, S., Liu, Y., Langrock, A., and Wang, C. (2013). Selenium@ mesoporous carbon composite with superior lithium and sodium storage capacity. ACS Nano *7*, 8003–8010.

Luo, C., Zhu, Y., Wen, Y., Wang, J., and Wang, C. (2014). Carbonized polyacrylonitrile-stabilized SeS_x cathodes for long cycle life and high power density lithium Ion batteries. Adv. Funct. Mater. *24*, 4082–4089.

Luo, C., Wang, J., Suo, L., Mao, J., Fan, X., and Wang, C. (2015). In situ formed carbon bonded and encapsulated selenium composites for Li-Se and Na-Se batteries. J. Mater. Chem. A *3*, 555–561.

Mukkabla, R., Deshagani, S., Meduri, P., Deepa, M., and Ghosal, P. (2017). Selenium/graphite platelet nanofiber composite for durable Li-Se batteries. ACS Energy Lett. *2*, 1288–1295.

Park, K., Cho, J.H., Jang, J.-H., Yu, B.-C., Andreah, T., Miller, K.M., Ellison, C.J., and Goodenough, J.B. (2015). Trapping lithium polysulfides of a Li-S battery by forming lithium bonds in a polymer matrix. Energy Environ. Sci. *8*, 2389–2395.

Park, S.-K., Park, J.-S., and Kang, Y.C. (2018). Selenium-infiltrated metal-organic framework-derived porous carbon nanofibers comprising interconnected bimodal pores for Li-Se batteries with high capacity and rate performance. J. Mater. Chem. A *6*, 1028–1036.

Singh, M., Kaiser, J., and Hahn, H. (2015). Thick electrodes for high energy lithium ion batteries. J. Electrochem. Soc. *162*, A1196–A1201.

Sun, H., Mei, L., Liang, J., Zhao, Z., Lee, C., Fei, H., Ding, M., Lau, J., Li, M., Wang, C., et al. (2017). Three-dimensional holey-graphene/niobia composite architectures for ultrahigh-rate energy storage. Science *356*, 599–604.

Sun, H., Zhu, J., Baumann, D., Peng, L., Xu, Y., Shakir, I., Huang, Y., and Duan, X. (2019). Hierarchical 3D electrodes for electrochemical energy storage. Nat. Rev. Mater. *4*, 45–60.

Talapaneni, S.N., Hwang, T.H., Je, S.H., Buyukcakir, O., Choi, J.W., and Coskun, A. (2016). Elemental-sulfur-mediated facile synthesis of a covalent triazine framework for high-performance lithium-sulfur batteries. Angew. Chem. Int. Ed. *55*, 3106–3111.

Tao, X., Wang, J., Liu, C., Wang, H., Yao, H., Zheng, G., Seh, Z.W., Cai, Q., Li, W., and Zhou, G. (2016). Balancing surface adsorption and diffusion of lithium-polysulfides on nonconductive oxides for lithium-sulfur battery design. Nat. Commun. *7*, 11203.

Wang, B., Zhang, J., Xia, Z., Fan, M., Lv, C., Tian, G., and Li, X. (2018). Polyaniline-coated selenium/carbon composites encapsulated in graphene as efficient cathodes for Li-Se batteries. Nano Res. *11*, 2460–2469.

Wang, T., Zhu, J., Wei, Z., Yang, H., Ma, Z., Ma, R., Zhou, J., Yang, Y., Peng, L., and Fei, H. (2019). Bacteria derived biological carbon building robust Li-S batteries. Nano Lett. *19*, 4384.

Xin, S., Gu, L., Zhao, N.-H., Yin, Y.-X., Zhou, L.-J., Guo, Y.-G., and Wan, L.-J. (2012). Smaller sulfur molecules promise better lithium-sulfur batteries. J. Mater. Chem. A *134*, 18510–18513.

Xin, S., Yu, L., You, Y., Cong, H.-P., Yin, Y.-X., Du, X.-L., Guo, Y.-G., Yu, S.-H., Cui, Y., and Goodenough, J.B. (2016). The electrochemistry with lithium versus sodium of selenium confined to slit micropores in carbon. Nano Lett. *16*, 4560–4568.

Yang, C.P., Xin, S., Yin, Y.X., Ye, H., Zhang, J., and Guo, Y.G. (2013). An advanced selenium-carbon cathode for rechargeable lithium-selenium batteries. Angew.Chem. Int. Ed. *52*, 8363–8367.

Yang, X., Wang, H., Yu, D.Y., and Rogach, A.L. (2018). Vacuum calcination Induced conversion of selenium/carbon wires to tubes for high-performance sodium-selenium batteries. Adv. Funct. Mater. *28*, 1706609.

Zeng, L., Wei, X., Wang, J., Jiang, Y., Li, W., and Yu, Y. (2015). Flexible one-dimensional carbon–selenium composite nanofibers with superior electrochemical performance for Li-Se/Na-Se batteries. J. Power Sources *281*, 461–469.

Zhang, S. (2014). Understanding of sulfurized polyacrylonitrile for superior performance lithium/sulfur battery. Energies *7*, 4588–4600.

Zhang, B., Qin, X., Li, G., and Gao, X. (2010). Enhancement of long stability of sulfur cathode by encapsulating sulfur into micropores of carbon spheres. Energy Environ. Sci. *3*, 1531–1537.

Zhang, J., Fan, L., Zhu, Y., Xu, Y., Liang, J., Wei, D., and Qian, Y. (2014). Selenium/interconnected porous hollow carbon bubbles composites as the cathodes of Li-Se batteries with high performance. Nanoscale *6*, 12952–12957.

Zhang, H., Jia, D., Yang, Z., Yu, F., Su, Y., Wang, D., and Shen, Q. (2017). Alkaline lignin derived porous carbon as an efficient scaffold for lithium-selenium battery cathode. Carbon *122*, 547–555.

Zhang, M., Shoaib, M., Fei, H., Wang, T., Zhong, J., Fan, L., Wang, L., Luo, H., Tan, S., and Wang, Y. (2019). Hierarchically porous N-Doped carbon fibers as a free standing anode for high-capacity potassium-based dual-ion battery. Adv. Energy Mater. *9*, 1901663.

iScience, Volume *23*

Supplemental Information

Covalent Selenium Embedded in Hierarchical Carbon Nanofibers for Ultra-High Areal Capacity Li-Se Batteries

Jian Zhou, Maoxin Chen, Tao Wang, Shengyang Li, Qiusheng Zhang, Meng Zhang, Hanjiao Xu, Jialing Liu, Junfei Liang, Jian Zhu, and Xiangfeng Duan

Supplemental Figures

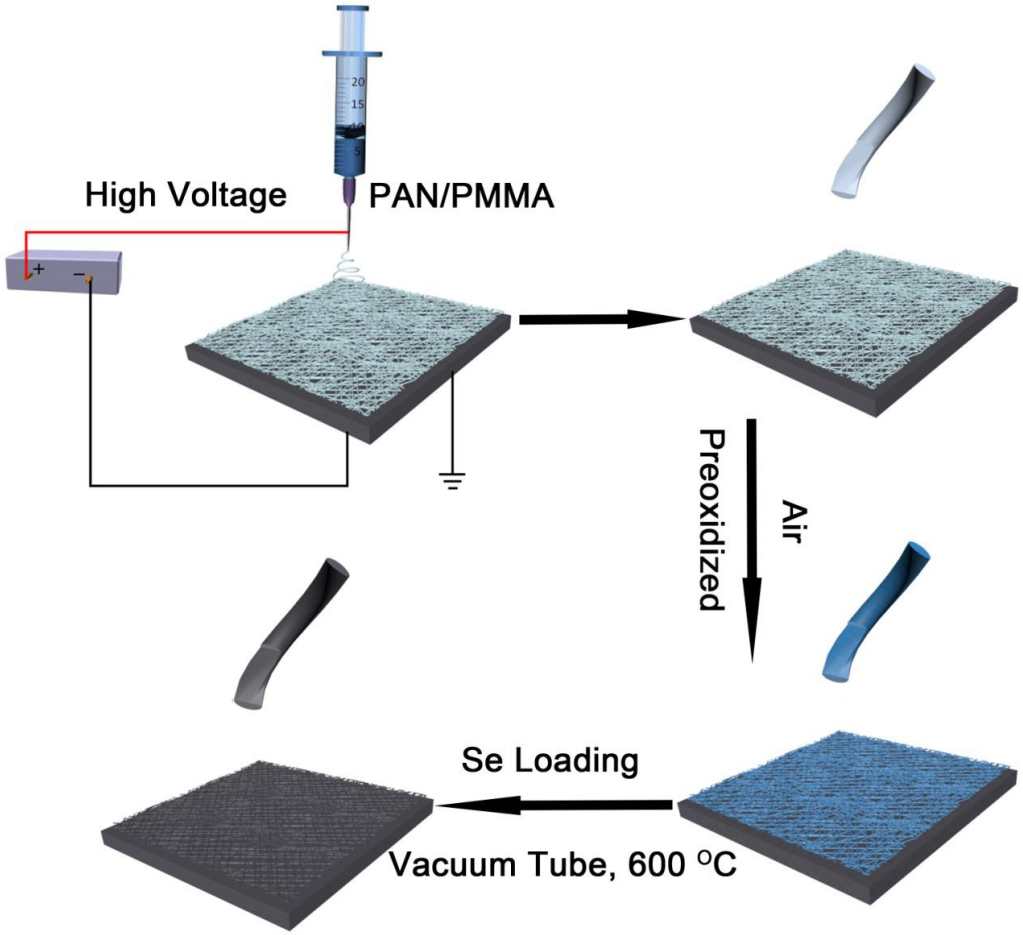

Figure S1. Schematic illustration of the synthesis process of the CSe@HNCNFs electrode.Related to Figure 1 and Figure 2.

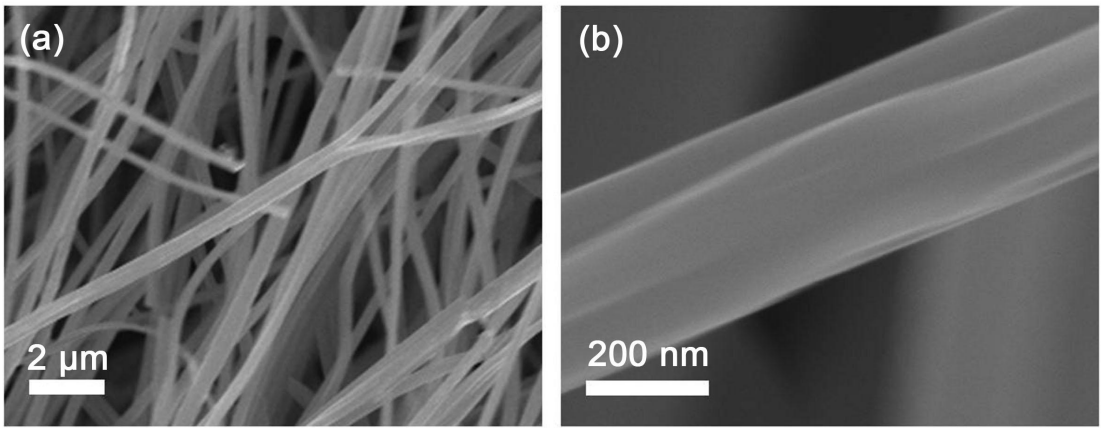

Figure S2. SEM images of (a) HNCNFs and corresponding (b) high magnification image. Related to Figure 1.

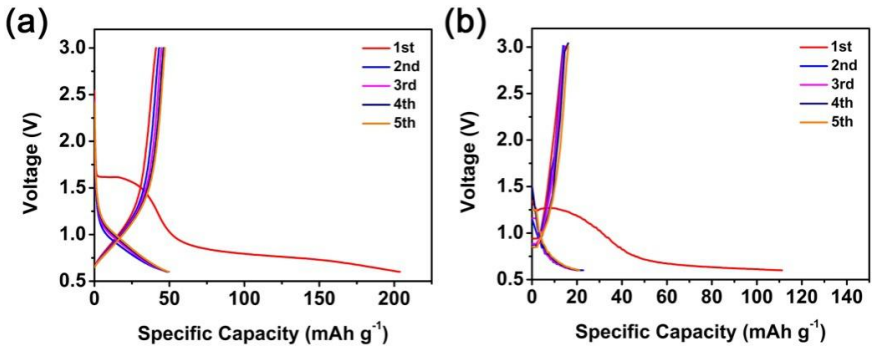

Figure S3. Galvanostatic charge-discharge profiles of the HNCNFs at a current density of (a) 0.1 and (b) 1 A g^{-1}. Related to Figure 3.

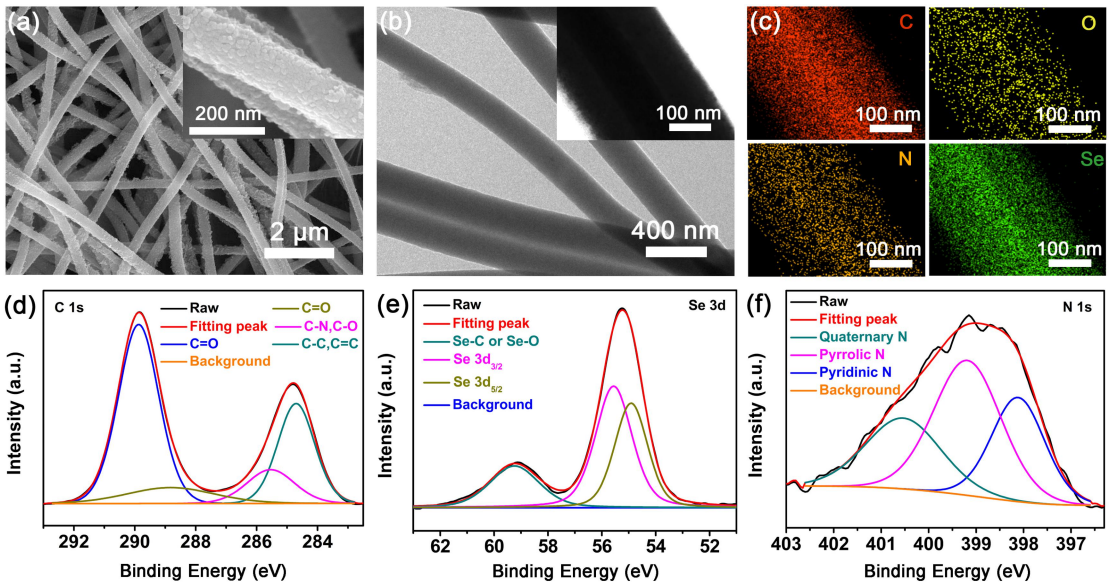

Figure S4. Morphological and composed characterizations of CSe@HNCNFs electrode after 400 cycles at C-rate 5 C. (a) SEM images. (b) TEM images. (c) Elemental mapping images for C, N, O and Se. (d, e and f) High-resolution XPS spectra of C 1s, Se 3d and N 1s for CSe@HNCNFs (Wang et al., 2019; Li et al., 2016; Luo et al., 2013; . Zhang et al., 2019; Delamar et al., 1992). Related to Figure 1 and Figure 3.

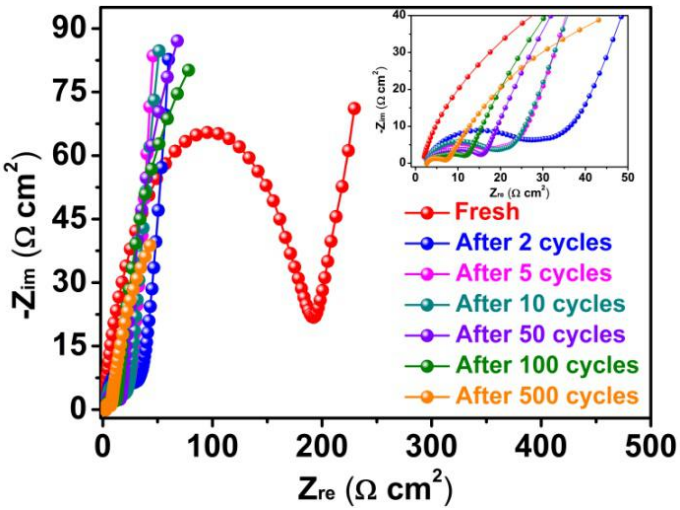

Figure S5. Nyquist plots of the fresh and cycled CSe@HNCNFSs electrode. Related to Figure 3.

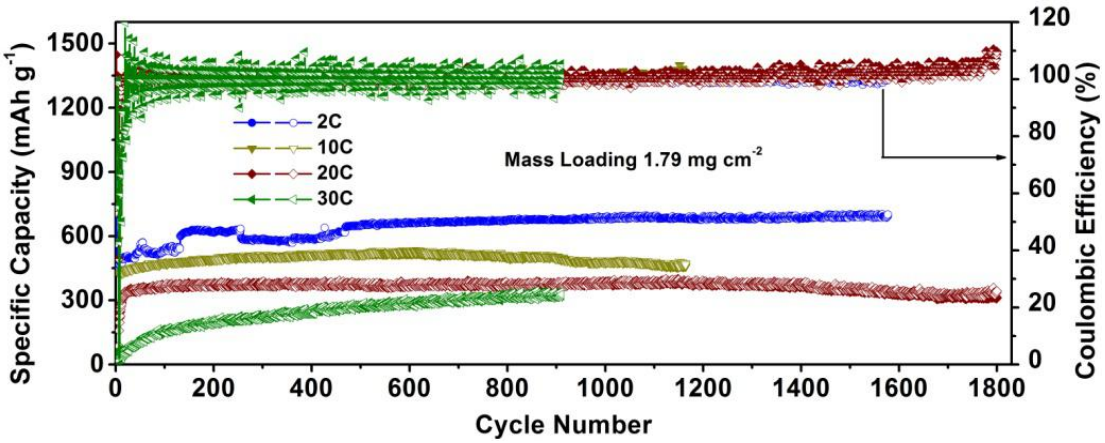

Figure S6. Cyclic performances and Coulombic efficiencies of the Se@MCNFs electrode at various current densities from 1 C to 30 C with mass loading of 1.79 mg cm^{-2}. Related to Figure 3.

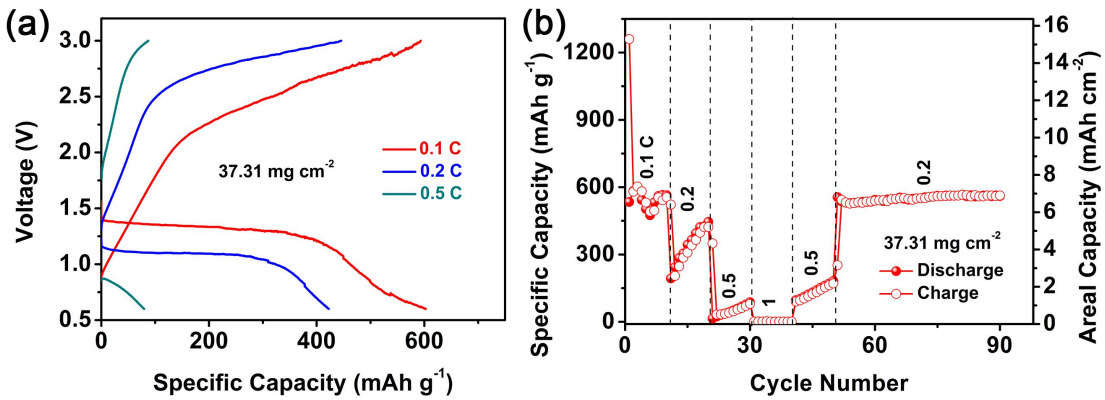

Figure S7. (a) Galvanostatic charge-discharge curves at different rates and (b) rate performance of CSe@HNCNFs electrode at mass loading of 37.31 mg cm^{-2} under different current rates from 0.1 to 1 C. Related to Figure 4.

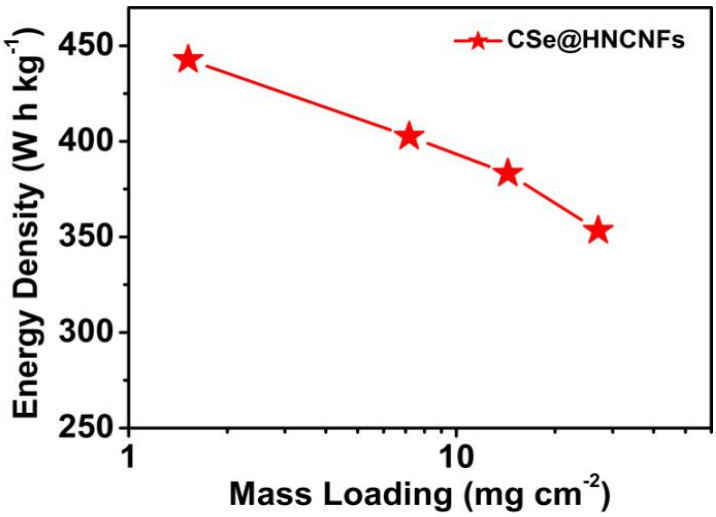

Figure S8. The gravimetric energy density trend graph under different mass loadings at the rate 0.2 C. Related to Figure 4.

Transparent Methods

Materials: In this study, all the chemicals were of analytical grade and without further purification.

Synthesis of the Pre-oxidized PAN/PMMA Nanofibers Film: In a typical process, 0.9 g polyacrylonitrile (PAN, M_w = 150000, Macklin) and 0.3 g polymethylmethacrylate (PMMA, M_w=996000, Sigma-Aldrich) were dissolved in 10 mL N,N-dimethylformamide (DMF, SCRC) at 75 °C under violent stirring for at least 24 hours. The obtained precursor solution was transferred into a 10 mL syringe, which was derived by a constant force with a flow rate of 0.8 mL h^{-1} to spray the PAN/PMMA nanofibers. The voltage of 18 kV and the distance of 15 cm were applied simultaneously between a 24-gauge blunt tip needle and a stainless steel collector. Finally，the collected PAN/PMMA nanofibers film was pre-oxidized in air at 280 °C for 3 h with a heating rate of 2 °C min^{-1}.

Synthesis of CSe@HNCNFs Film Composite: In order to obtain the CSe@HNCNFs, 0.3 g pre-oxidized PAN/PMMA nanofibers paper and 0.3 g selenium were vacuum-sealed in a glass tube. Then the vacuum glass tube was annealed at 600 °C for 10 h with a heating rate of 1 °C min^{-1}. After the above process, the CSe@HNCNFs film composite was obtained.

Material Characterization: The surface morphologies of the composites were investigated via SEM (Zeiss, Germang) and TEM (FEI Tecnai G2 F20, operating at 200 kV, America). Energy-dispersive X-ray spectroscopy (DEX, FP 9761-70, America) were used for analyzing elemental mapping. XRD studies were carried out using an XRD-6100 (Shimadzu，Japan) with Cu Kα radiation (λ = 1.5406 Å) over a 2θ range of 10°-80°. Raman spectra were collected from CSe@HNCNFs composite using a confocal microscope (invia - reflex, Renishaw) with 633 nm laser as the excitation. XPS studies were performed using a SCALAB 250Xi spectrometer (Thermo Fisher Scientific, America) with monochromatic Mg Ka radiation. Thermogravimetric analysis (TGA, STA 409 PC/4/H, Germang) were collected in nitrogen from room temperature to 700 °C at a heating rate of 10 °C min^{-1}. BET surface area and DFT pore size distribution tests were carried out by Micromeritics ASAP 2020 HD88 (Mack, America).

Electrochemical Measurements: CR2032-type coin cells were assembled to evaluate the

electrochemical properties of the CSe@HNCNFs composite for rechargeable Li-Se batteries. The CSe@HNCNFs film was directly cut into round slices with a diameter of 12 mm and then weighed in a high-precision analytical balance with an areal mass loading ranging from 1.52 to 27.12 mg cm^{-2}. The Polypropylene (PP), lithium foil and 1.0 M LiTFSI dissolved in 1,4-dioxolane/1,2-dimethoxyethane (V_{DOL}:V_{DME}= 1:1) with 1 wt% $LiNO_3$ additive were used as separator, anode and electrolyte, respectively. Charge-discharge performance was performed on a CT2001A battery testing system (Wuhan LAND Electronic). In addition, CV measurements and electrochemical impedance spectroscopy (EIS) were carried out on a CHI660E (Shanghai CH Instrument) electrochemical workstation. The CV measurements were performed at the voltage window of 0.6-3.0 V **(***vs.* Li/Li^+). The EIS measurements were performed with a sinusoidal signal in frequency range from 100 kHz to 10 mHz at an amplitude of 5 mV. All specific capacity in this work was calculated according to the mass of selenium.

The gravimetric energy density E_g is calculated according to the following equation:

$$E_g = Q_e \cdot U$$

Where Q_e (mAh g^{-1}) is the discharge capacity of the CSe@HNCNFs electrode; U (V) is discharge plateau.

References

Luo, C., Xu, Y., Zhu, Y., Liu, Y., Zheng, S., Liu, Y., Langrock, A., and Wang, C. (2013). Selenium@mesoporous carbon composite with superior lithium and sodium storage capacity. ACS nano *7*, 8003-8010.

Wang, T., Zhu, J., Wei, Z., Yang, H., Ma, Z., Ma, R., Zhou, J., Yang, Y., Peng, L., and Fei, H. (2019). Bacteria derived biological carbon building robust Li-S batteries. Nano lett. *19,* 4384.

Li, G., Sun, J., Hou, W., Jiang, S., Huang, Y., and Geng, J. (2016). Three-dimensional porous carbon composites containing high sulfur nanoparticle content for high-performance lithium-sulfur batteries. Nat. commun. *7,* 10601.

Zhang, M., Shoaib, M., Fei, H., Wang, T., Zhong, J., Fan, L., Wang, L., Luo, H., Tan, S., and Wang, Y. (2019). Hierarchically porous N-Doped carbon fibers as a free standing anode for high-capacity potassium-based dual-ion battery. Adv. Energy Mater. *9*, 1901663.

Delamar, M., Hitmi, R., Pinson, J., and Saveant, J. M. (1992). Covalent modification of carbon surfaces by grafting of functionalized aryl radicals produced from electrochemical reduction of diazonium salts. J. Am. Chem. Soc. *114,* 5883-5884.